To appear in the *International Journal of Remote Sensing*
Vol. 00, No. 00, Month 20XX, 1–15

Multispectral Super-Resolution of Tropical Cyclone Imagery using Sparsity-based Approaches

I. Yanovsky[a*] and B. Lambrigtsen[b]

[a] *Jet Propulsion Laboratory, California Institute of Technology, Pasadena, CA 91109, USA*; [b] *University of California, Los Angeles, Joint Institute for Regional Earth System Science and Engineering, Los Angeles, CA 90095, USA*

(*April 5, 2016*)

An aperture synthesis system produces ringing at sharp edges and other transitions in the observed field. In this paper, we have developed an efficient multispectral deconvolution method, based on Split Bregman total variation minimization technique, and showed it to reduce image ringing, blurring, and distortion, while sharpening the image and preserving information content. We also present a multispectral multiframe super-resolution method that is robust to image noise and noise in the point spread function and leads to additional improvements in spatial resolution. The methodologies are based on current research in sparse optimization and compressed sensing, which lead to unprecedented efficiencies for solving image reconstruction problems.

Keywords: Aperture synthesis system, inverse problems, microwave imaging, multispectral image analysis, remote sensing, spatial resolution, super-resolution.

1. Introduction

Physically deforming phenomena, such as hurricanes and tropical storms, will soon be continuously captured using geostationary microwave sensors. These sensors are designed to penetrate through thick clouds to see the structure of a storm. The images collected are valuable for evaluating the storm's internal processes and its strength.

The Geostationary Synthetic Thinned Aperture Radiometer (GeoSTAR) is a microwave spectrometer aperture synthesis system that will be used to capture hurricane imagery (Tanner et al. 2007). A characteristic of an aperture synthesis system is that the point spread function (PSF) is a 2-dimensional sinc-like function, showing positive and negative excursions (cf. Fig. 3), that produces ringing at sharp edges and other transitions in the observed field. The conventional approach to suppressing such sidelobes is to apply linear apodization, which has the undesirable side effect of degrading spatial resolution (Tanner and Swift 1993; Yanovsky et al. 2015).

In order to reduce image ringing while sharpening the image and preserving information content, we formally solved the deconvolution inverse problem for single-

*Corresponding author. Email: igor.yanovsky@jpl.nasa.gov. This is an Accepted Manuscript of an article published by Taylor & Francis in the International Journal of Remote Sensing on May 9, 2016, available at http://www.tandfonline.com/doi/full/10.1080/01431161.2016.1177245.

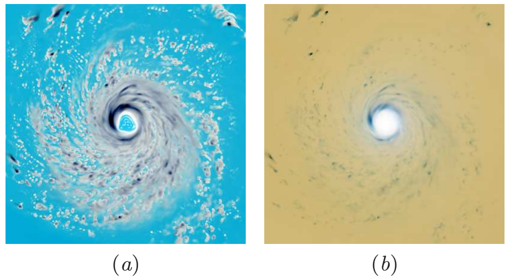

Figure 1. Original microwave channels of the simulated hurricane Rita image are displayed as red-green-blue images for (*a*) (50.3, 52.8, 53.6) GHz, and (*b*) (54.4, 54.94, 55.5) GHz.

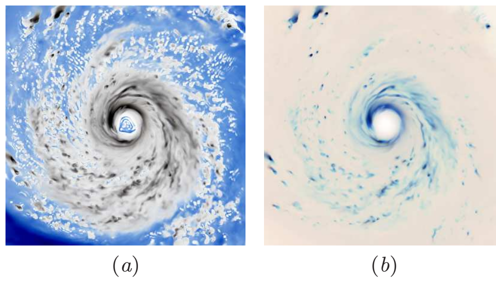

Figure 2. Original microwave channels of the simulated hurricane Rita image are displayed as red-green-blue images for (*a*) (150, 157, 166) GHz, and (*b*) (176.31, 180.31, 182.31) GHz.

channel images in (Yanovsky et al. 2015). Since the convolution problem in the presence of noise is highly ill-posed, regularization was applied to achieve stability while preserving a priori properties of the solution. We formulated the restoration problem within the variational framework, using the total variation regularization (Rudin, Osher, and Fatemi 1992). Total variation (TV) of an image measures the sum of the absolute values of its gradient and increases in the presence of the ringing artifact caused by sidelobes. By minimizing the TV, we showed that the process reduces not only the ringing within the image, but also significantly reduces the brightness temperature errors in the overall image. These processes were rendered efficiently by employing methodologies based on current research in sparse optimization and compressed sensing. We performed the total variation based deconvolution within the Split Bregman optimization framework to achieve a significant computational time improvement over already robust total-variation gradient descent based techniques. In this paper, we generalize an efficient TV-based Split Bregman deconvolution method to efficiently reconstruct multispectral imagery.

Split Bregman method can be derived from the well-known alternating direction method of multipliers (ADMM) (Glowinski and Marrocco 1975; Gabay and Mercier 1976; Glowinski, Lions, and Tremolieres 1981) and is very efficient because it can decompose a non-smooth multi-term optimization problems into subproblems with closed-form solutions. This advantage for total variation regularization problems was first discovered in (Wang et al. 2008) for image denoising and deblurring, and has been generalized to multichannel problems in (Yang et al. 2009), the TV-L1 model in (Yang, Zhang, and Yin 2009), TV-based compressed sensing in (Goldstein and Osher 2009; Yang, Zhang, and Yin 2010), and an edge guided compressive sensing reconstruction approach for recovering images of higher qualities from fewer measurements in (Guo and Yin 2012).

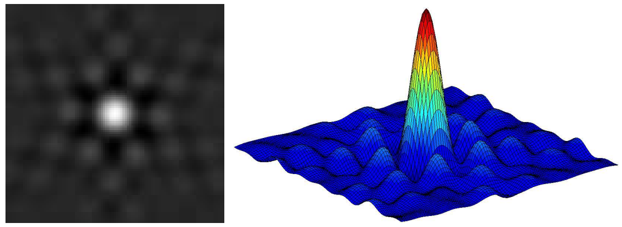

Figure 3. (*a*) The GeoSTAR PSF shown as image. A characteristic of an aperture synthesis system is that the PSF is a 2-dimensional sinc-like function, showing positive and negative excursions, that produces ringing at sharp edges and other transitions in the observed field. (*b*) The GeoSTAR PSF shown as surface.

2. Notation

We first introduce notations that will be used throughout this paper.

- For a *single-channel* image $u \in \mathbb{R}^{n\times n}$, the value of u at a pixel (i,j), with $0 \le i,j \le n$, is denoted as $u_{i,j}$. The norms are defined as:

$$||u||_1 = \sum_{(i,j)\in\Omega} |u_{i,j}|, \qquad ||u||_2 = \sqrt{\sum_{(i,j)\in\Omega} |u_{i,j}|^2},$$

where Ω is an image domain. The gradient of u is denoted as ∇u and its value at pixel (i,j) as $(\nabla u)_{i,j}$, with $(\nabla u)_{i,j} \in \mathbb{R}^2$. Consider scalar-valued functions d_1 and d_2. For a vector-valued quantity $\boldsymbol{d}_{i,j} = ((d_1)_{i,j}, (d_2)_{i,j}) \in \mathbb{R}^2$ (e.g. $\boldsymbol{d} = \nabla u$), the norms are defined as

$$||\boldsymbol{d}||_1 = \sum_{(i,j)\in\Omega} ||\boldsymbol{d}_{i,j}||_2, \qquad ||\boldsymbol{d}||_2 = \sqrt{\sum_{(i,j)\in\Omega} ||\boldsymbol{d}_{i,j}||_2^2}, \tag{1}$$

where $||\boldsymbol{d}_{i,j}||_2 = \sqrt{(d_1)_{i,j}^2 + (d_2)_{i,j}^2}$. Unless specified otherwise, $||\cdot|| = ||\cdot||_2$ in the remainder of this paper.

- For a *multichannel* image $\boldsymbol{u} \in (\mathbb{R}^{n\times n})^C$, with C channels, $\boldsymbol{u}$ is written as $\boldsymbol{u} = (u^{(1)}, u^{(2)}, \cdots, u^{(C)})$. Each $u^{(c)}$, $c = 1,\ldots,C$, is a single-channel image. The value of $\boldsymbol{u}$ at a pixel (i,j), with $0 \le i,j \le n$, is denoted as $\boldsymbol{u}_{i,j} = (u_{i,j}^{(1)}, u_{i,j}^{(2)}, \cdots, u_{i,j}^{(C)})$. The norms are defined as:

$$||\mathbf{u}||_1 = \sum_{(i,j)\in\Omega} \left(|u_{i,j}^{(1)}| + \ldots + |u_{i,j}^{(C)}|\right),$$

$$||\mathbf{u}||_2 = \sqrt{\sum_{(i,j)\in\Omega} (u_{i,j}^{(1)})^2 + \ldots + (u_{i,j}^{(C)})^2}.$$

We denote the generalization of the gradient for a multichannel image $\boldsymbol{u}$ as $\nabla\boldsymbol{u}$ and its value at pixel (i,j) as $(\nabla\boldsymbol{u})_{i,j}$, with $(\nabla\boldsymbol{u})_{i,j} \in \mathbb{R}^{2C}$. For $\boldsymbol{d} = \nabla\mathbf{u}$, the norms are defined as in (1), with $||\boldsymbol{d}_{i,j}||_2 = \sqrt{(d_1)_{i,j}^2 + \ldots + (d_{2C})_{i,j}^2}$.

- The following signal-to-noise ratio (SNR) and root mean square error (RMSE)

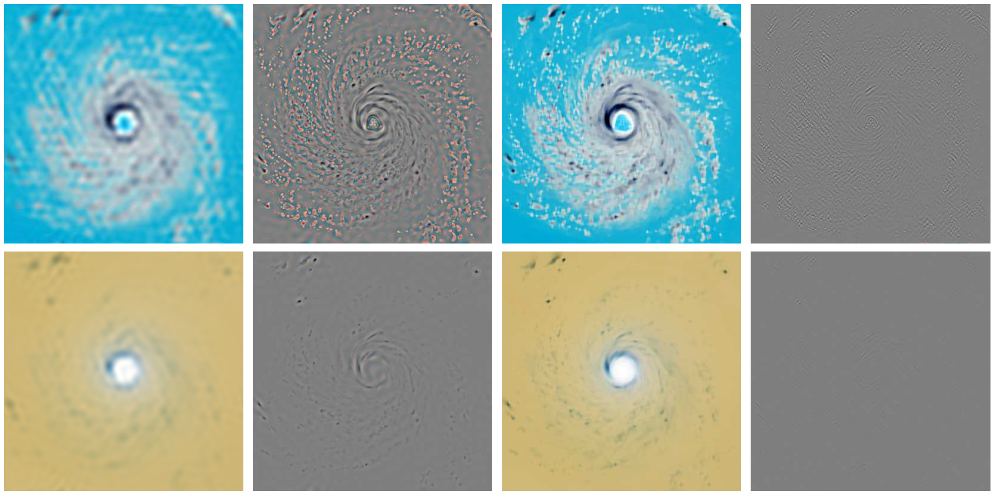

Figure 4. Multispectral reconstruction of simulated hurricane images using Split Bregman deconvolution. The two rows represent different microwave channels as RGB color images: (50.3, 52.8, 53.6) GHz and (54.4, 54.94, 55.5) GHz, respectively. Note that the multispectral reconstruction is performed over all six channels, and three-channel RGB images are shown only for visualization purposes. (*a*) Original microwave channels from Figure 1 are convolved with GeoSTAR kernel from Figure 3. (*b*) Errors in convolved images. (*c*) Deconvolution results. (*d*) Errors in reconstructed results.

were employed as quantitative measures:

$$\mathrm{SNR} \;=\; 10\log_{10}\left(\frac{\sigma^2_{\boldsymbol{u}_0} n^2}{\sum_{c=1}^{C} ||u_0^{(c)} - u^{(c)}||^2}\right), \tag{2}$$

$$\mathrm{RMSE} \;=\; \sqrt{\frac{1}{Cn^2}\sum_{c=1}^{C}\sum_{(i,j)\in\Omega} |u_{0\,i,j}^{(c)} - u_{i,j}^{(c)}|^2}, \tag{3}$$

where C is the number of channels, n^2 is the total number of pixels in the image, $\boldsymbol{u}_0 = (u_0^{(1)}, u_0^{(2)}, \cdots, u_0^{(C)})$ represents the original multichannel clean image, $\sigma^2_{\boldsymbol{u}_0}$ is the variance of $\boldsymbol{u}_0$, and $\boldsymbol{u}$ represents the image of interest.

3. Multispectral Deconvolution

The standard linear degradation model for a blurry and noisy multichannel observation $\boldsymbol{f}$ is given as

$$\boldsymbol{f} = K * \boldsymbol{u}_0 + \kappa, \tag{4}$$

where $*$ denotes convolution operator, K is a kernel, κ is additive noise, and $\boldsymbol{u}_0$ is a clean unknown image. For an aperture synthesis system, K is a sinc-like point spread function which introduces sidelobes in the observation. Rather than apply the conventional linear apodization approach, which has the undesirable side effect of degrading spatial resolution (Tanner and Swift 1993), we suppress interferometric sidelobes by constructing a variational formulation for image reconstruction and solving an inverse problem. Regularization is applied within a variational framework in order to achieve stability while preserving a priori properties of the solution. New image restoration models, based on non-local image information, have been

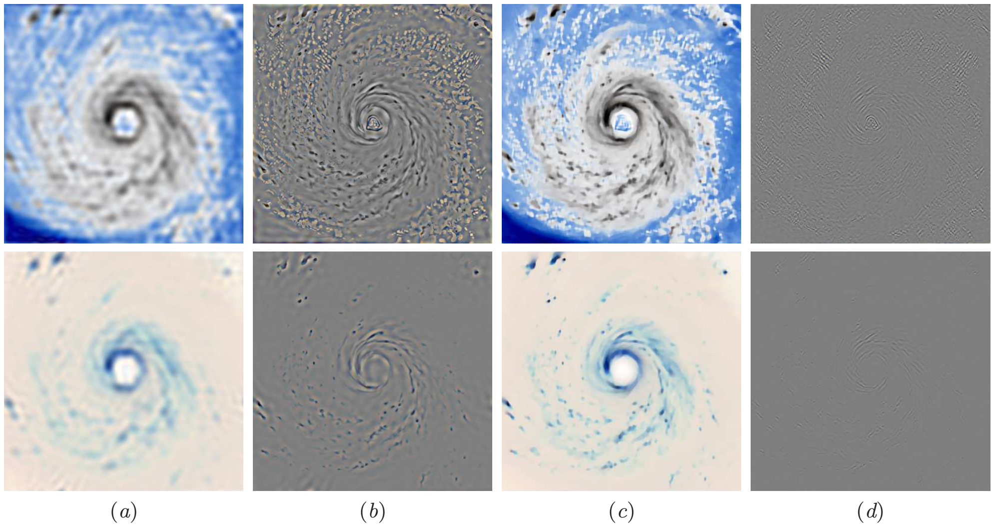

Figure 5. Multispectral reconstruction of simulated hurricane images using Split Bregman deconvolution. The two rows represent different microwave channels as RGB color images: (150, 157, 166) GHz and (176.31, 180.31, 182.31) GHz, respectively. Note that the multispectral reconstruction is performed over all six channels, and three-channel RGB images are shown only for visualization purposes. (*a*) Original microwave channels from Figure 2 are convolved with GeoSTAR kernel from Figure 3. (*b*) Errors in convolved images. (*c*) Deconvolution results. (*d*) Errors in reconstructed results.

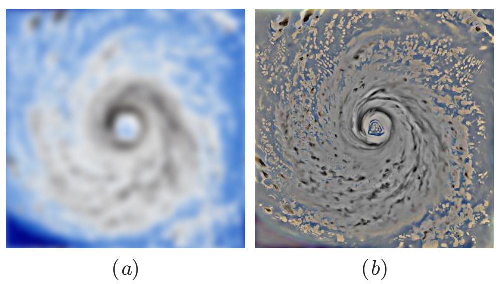

Figure 6. (*a*) Result obtained after applying the conventional linear apodization method on image of Figure 5(*a*, top). (*b*) Corresponding error is shown. SNR = 34.07 and RMSE = 19.96K. Linear apodization method raises the errors relative to Figure 5(*b*, top).

developed (Gilboa and Osher 2007, 2008; Peyré 2008; Szlam, Maggioni, and Coifman 2008; Lou et al. 2010; Buades, Coll, and Morel 2005; Kindermann, Osher, and Jones 2005). In particular, in (Jung et al. 2009, 2011), the authors proposed the Mumford-Shah based model (Mumford and Shah 1989) which uses nonlocal image information. However, such approaches are very computationally expensive.

In (Yanovsky et al. 2015), by formally solving the deconvolution inverse problem for single-channel images, we reduced image ringing inherent in aperture synthesis system, while sharpening the image and preserving information content. We used the L_1-regularized type norm $||u||_{\mathrm{TV}} = \int |\nabla u|$, which measures the total variation (TV). The minimization of the TV norm does not penalize edges in an image. In this paper, we minimize the deconvolution problem within an efficient multispectral total variation based Split Bregman minimization framework.

The generalization of the TV norm to multispectral framework is the multichannel total variation (MTV), and is given as

$$||\boldsymbol{u}||_{\mathrm{MTV}} = \sum_{(i,j)\in\Omega} \sqrt{||(\nabla u^{(1)})_{i,j}||^2 + \cdots + ||(\nabla u^{(C)})_{i,j}||^2}. \tag{5}$$

Given a single observation $\boldsymbol{f}$, we solve the inverse problem. The minimization problem for MTV-L_2 deconvolution can be written as

$$\min_{\boldsymbol{u}} \quad ||\boldsymbol{u}||_{\text{MTV}} + \frac{\mu}{2}||K * \boldsymbol{u} - \boldsymbol{f}||_2^2, \tag{6}$$

where the second term is the L_2 norm of the residual of (4), $\mu > 0$ is a weight, and $\boldsymbol{u}$ is a reconstruction.

The Split Bregman formulation minimizes (6) by introducing an additional variable $\boldsymbol{d}$ in order to transfer $\nabla \boldsymbol{u}$ out of non-differentiable terms at each pixel:

$$\min_{\boldsymbol{u},\boldsymbol{d}} \quad ||\boldsymbol{d}||_1 + \frac{\lambda}{2}||\boldsymbol{d} - \nabla \boldsymbol{u} - \boldsymbol{b}||^2 + \frac{\mu}{2}||K * \boldsymbol{u} - \boldsymbol{f}||^2. \tag{7}$$

Here, λ is a nonnegative parameter, and variable $\boldsymbol{b}$ is chosen through Bregman iteration (Yin et al. 2008; Osher et al. 2005):

$$\boldsymbol{b} \leftarrow \boldsymbol{b} + (\nabla \boldsymbol{u} - \boldsymbol{d}). \tag{8}$$

For a fixed $\boldsymbol{u}$, the minimization problem for $\boldsymbol{d}$ is

$$\boldsymbol{d}^* = \arg\min_{\boldsymbol{d}} \left\{ ||\boldsymbol{d}||_1 + \frac{\lambda}{2}||\boldsymbol{d} - \nabla \boldsymbol{u} - \boldsymbol{b}||^2 \right\}, \tag{9}$$

which can be explicitly solved for $\boldsymbol{d}$, at each pixel, by using a generalized shrinkage formula (Donoho and Johnstone 1995; Wang, Yin, and Zhang 2007).

For a fixed $\boldsymbol{d}$, the minimization problem (7) is quadratic in $\boldsymbol{u}$:

$$\boldsymbol{u}^* \ = \ \arg\min_{\boldsymbol{u}} \left\{ ||\boldsymbol{d} - \nabla \boldsymbol{u} - \boldsymbol{b}||^2 + \frac{\mu}{\lambda}||K * \boldsymbol{u} - \boldsymbol{f}||^2 \right\},$$

and has the optimality condition:

$$\mu \tilde{K} * K * \boldsymbol{u} - \lambda \triangle \boldsymbol{u} = \mu \tilde{K} * \boldsymbol{f} - \lambda \nabla \cdot (\boldsymbol{d} - \boldsymbol{b}), \tag{10}$$

where $\tilde{K}(x) = K(-x)$. We solve (10) using the fast Fourier transform. Algorithm 1 below is a high level description of the method.

Algorithm 1 Split Bregman Isotropic TV Deconvolution

1: Initialize $\boldsymbol{u} = \boldsymbol{f}$, $\boldsymbol{d} = \boldsymbol{0}$, $\boldsymbol{b} = \boldsymbol{0}$.
2: Solve (9) for $\boldsymbol{d}$.
3: Update $\boldsymbol{b}$ as in (8).
4: Solve (10) for $\boldsymbol{u}$.
5: Repeat from step 2.

We tested the method on simulated microwave images of the 2005 Atlantic hurricane Rita, shown in Figures 1 and 2. Figure 1 shows 50.3, 52.8, 53.6, 54.4, 54.94, 55.5 GHz channels as color images (three channels per color image). These six channels correspond to the AMSU-A channels. Figure 2 shows 150, 157, 166, 176.31, 180.31, 182.31 GHz channels as color images. These six channels correspond to the AMSU-B water vapor sounding channels, which are placed progressively closer to the 183 GHz water vapor resonance frequency to provide a range of penetration

Table 1. Signal-to-noise ratios of blurry and reconstructed images shown in Figures 4, 5, and 8

	SNR	
Image	Blurry image	Reconstructed image
AMSU-A (Figure 4)	34.71	41.80
AMSU-B (Figure 5)	35.49	42.97
TC Katrina (Figure 8)	37.04	50.44
TC Rita (Figure 8)	36.91	50.44
TC Talim (Figure 8)	40.63	52.40

Table 2. Root mean square errors in blurry and reconstructed images shown in Figures 4, 5, and 8

	RMSE	
Image	Blurry image	Reconstructed image
AMSU-A (Figure 4)	15.34	6.78
AMSU-B (Figure 5)	16.96	7.17
TC Katrina (Figure 8)	11.66	2.49
TC Rita (Figure 8)	11.61	2.44
TC Talim (Figure 8)	7.51	1.93

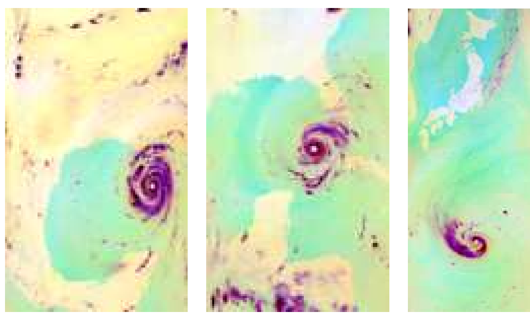

(*a*) (*b*) (*c*)

Figure 7. Original AMSU-B channels capturing tropical cyclones (TC) (*a*) Katrina, (*b*) Rita, and (*c*) Talim are displayed as red-green-blue images.

depths. These channels are later combined with temperature profiles to resolve the vertical distribution of water vapor in the atmosphere. For comparison, GeoSTAR operates at some of the same frequencies of the Advanced Microwave Sounding Unit - A (AMSU-A) and - B (AMSU-B) temperature and humidity sounders near 55 GHz and 180 GHz, respectively. The images have a size of 400×400 pixels and were derived from cloud resolving numerical weather prediction model (WRF) (Michalakes et al. 1998) simulations. The resolution of a pixel is 1.3 km. With this grid spacing, we can resolve features that are approximately 5 km wide. We used the 101×101 GeoSTAR point spread function K, which has a full width at half maximum of 27.6 km and is shown in Figure 3, to blur the images.

Figure 4(a) shows the multispectral images of Figure 1 degraded with the GeoSTAR blur. These six channels (between 50.3 and 55.5 GHz) correspond to some of the frequencies of AMSU-A. The result in Figure 4(c) is obtained using the efficient multispectral Split Bregman deconvolution model. Note that even though Figure 4(c) shows three channels per image, multispectral reconstruction was performed on all six channels simultaneously. Figures 4(b,d) show the original error and error after reconstruction and Tables 1 and Table 2 give signal-to-noise ratio (SNR) and root mean square (RMS) error values (see (2) and (3)), respectively. These error measures are relative to the original image in Figure 1. In Figure 4(c),

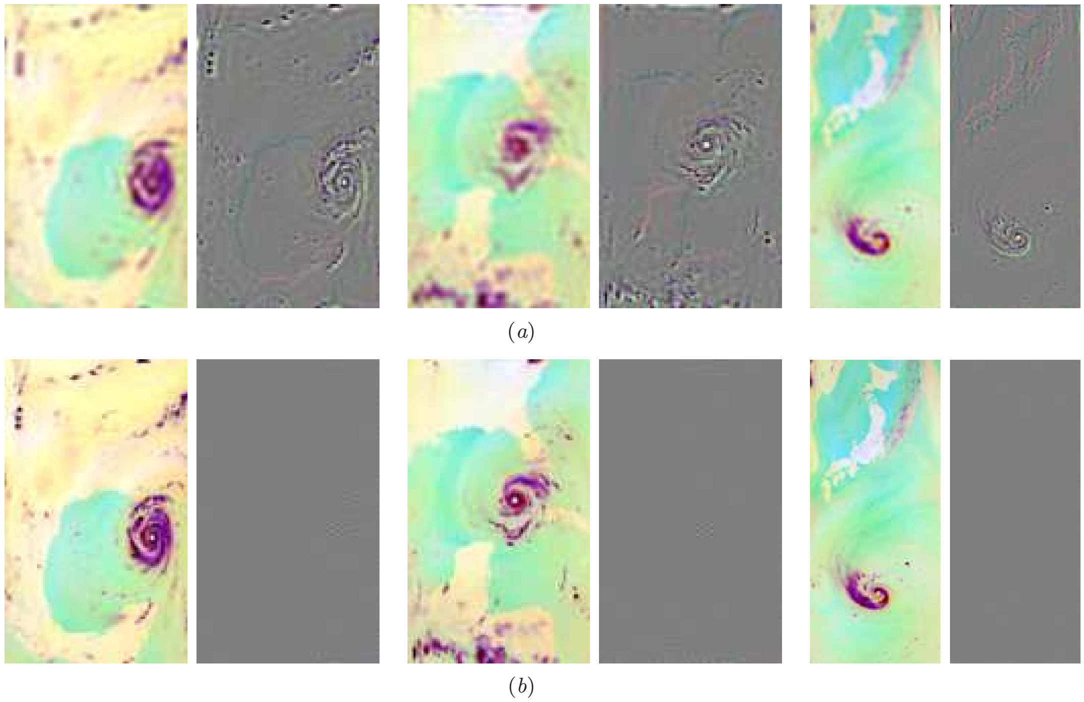

Figure 8. Multispectral reconstruction of real tropical cyclone images using Split Bregman deconvolution. Different microwave channels are represented as RGB color images. Note that the multispectral reconstruction is performed over all five AMSU-B channels, and three-channel RGB images are shown only for visualization purposes. (a) Original microwave channels from Figure 7 are convolved with GeoSTAR kernel from Figure 3. Initial errors are also shown. (b) Reconstructed images and corresponding errors. Columns of this figure show tropical cyclone Katrina and corresponding errors, tropical cyclone Rita and corresponding errors, and tropical cyclone Talim and corresponding errors.

the proposed technique has produced an image which appears to match the true image, and also in Figure 4(d) truly reduces image errors compared to Figure 4(b).

Similarly, Figure 5(a) shows the multispectral images of Figure 2 degraded with the GeoSTAR blur. These six channels (between 150 and 182.31 GHz) correspond to some of the frequencies of AMSU-B. The result in Figure 5(c) is obtained using the efficient multispectral Split Bregman deconvolution model. Figures 5(b,d) show the original error and error after reconstruction and Tables 1 and Table 2 give SNR and RMS error values, respectively. As expected, the deconvolution model decreases the errors. On the other hand, apodization (see Figure 6) raises the errors relative to Figure 5(b,top) (Tanner and Swift 1993).

Figure 7 shows multispectral AMSU-B images capturing 2005 tropical cyclones (TC) Katrina, Rita, and Talim. Figure 8(a) shows the multispectral images of Figure 7 degraded with the GeoSTAR blur. Initial errors are also shown on this figure. The result in Figure 8(b) is obtained using the multispectral Split Bregman deconvolution model. Errors after reconstruction are also shown on this figure. Tables 1 and Table 2 give SNR and RMS error values, respectively. Figure 9 shows all five original AMSU-B channels capturing TC Katrina, TC Rita, and TC Talim. Figures 10(a), 11(a), and 12(a) display images of Figure 9 degraded with the GeoSTAR blur. Figures 10(b), 11(b), and 12(b) display results obtained using multispectral Split Bregman deconvolution model.

We also assessed computational efficiency of the fast fourier transform-based Split Bregman deconvolution method and found that solving the deconvolution problem using the fast Split Bregman method is over five hundred times faster than using the gradient descent method.

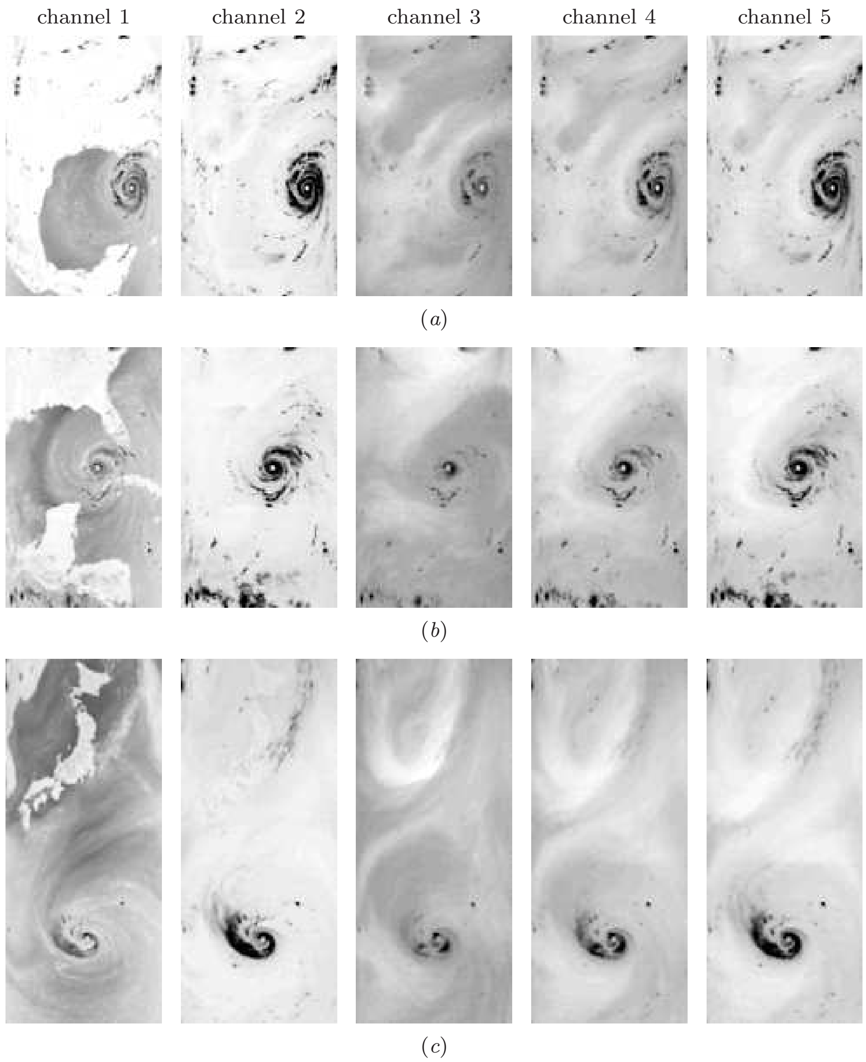

Figure 9. All five original AMSU-B channels capturing tropical cyclones (TC) (*a*) Katrina, (*b*) Rita, and (*c*) Talim are displayed.

4. Multispectral Multiframe Super-resolution

Multiframe super-resolution reconstruction produces a high-resolution image from a sequence of blurry and noisy low-resolution images. Given multiple noisy and blurry multispectral observations $\boldsymbol{f}_k$, where $k = 1, \ldots, Q$, we assume the point spread function K contains noise s_k. The convolution model describing the relation between the unknown clean image u_0 and each of the corrupted observations $\boldsymbol{f}_k$ is given by

$$\boldsymbol{f}_k = (K + s_k) * \boldsymbol{u}_0 + \kappa_k,$$

where κ_k is image noise. A conceptual diagram of multiframe super-resolution process, which involves PSF degraded with different noise functions for each frame, is shown in Figure 13.

We consider the following minimization problem for multispectral multiframe

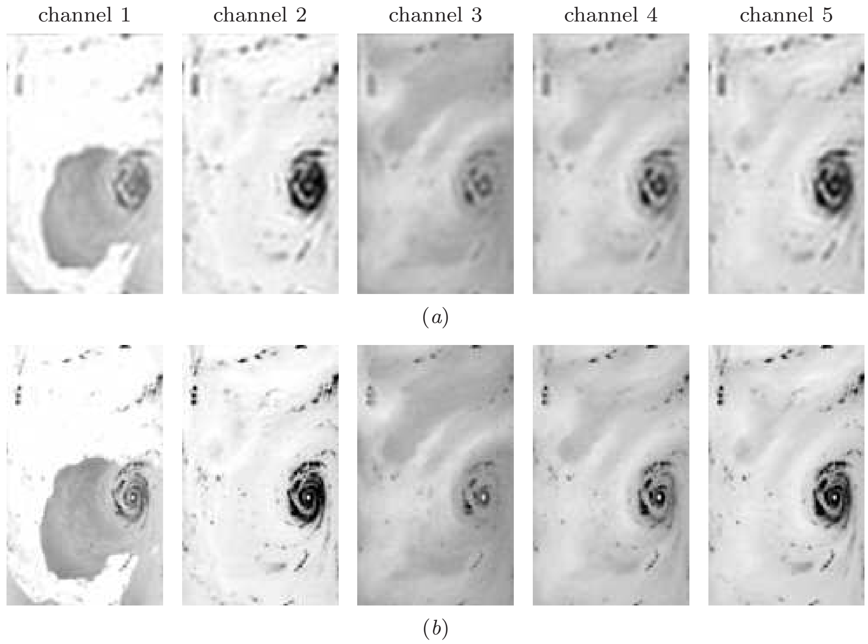

Figure 10. Multispectral reconstruction of channels capturing tropical cyclone Katrina. (a) Original microwave channels from Figure 9(a) are convolved with GeoSTAR kernel from Figure 3. (b) Reconstructed images.

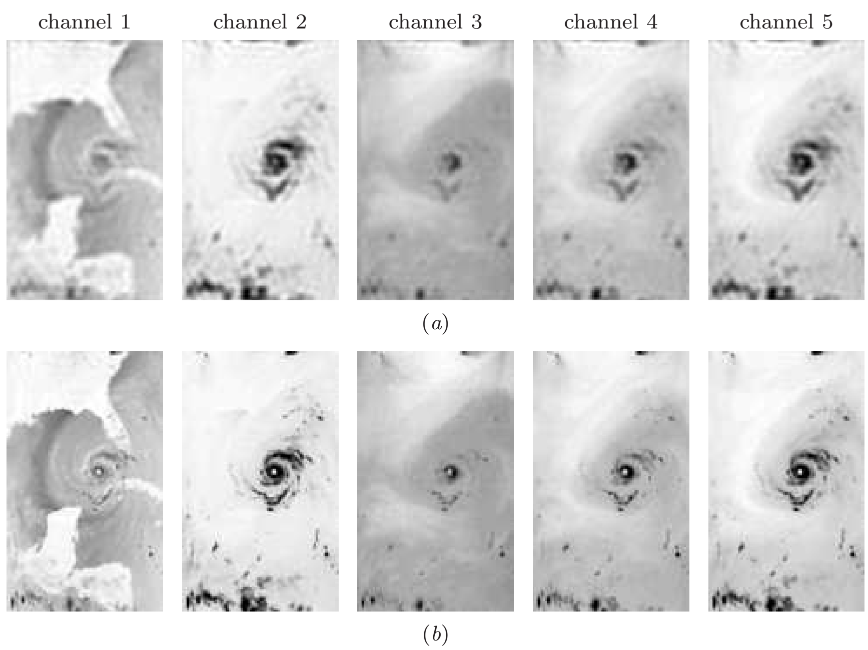

Figure 11. Multispectral reconstruction of channels capturing tropical cyclone Rita. (a) Original microwave channels from Figure 9(b) are convolved with GeoSTAR kernel from Figure 3. (b) Reconstructed images.

super-resolution:

$$\min_{\boldsymbol{u}} \quad ||\boldsymbol{u}||_{\mathrm{MTV}} + \frac{\mu}{2}\sum_{k=1}^{Q}\omega_k ||K * \boldsymbol{u} - \boldsymbol{f}_k||_2^2. \tag{11}$$

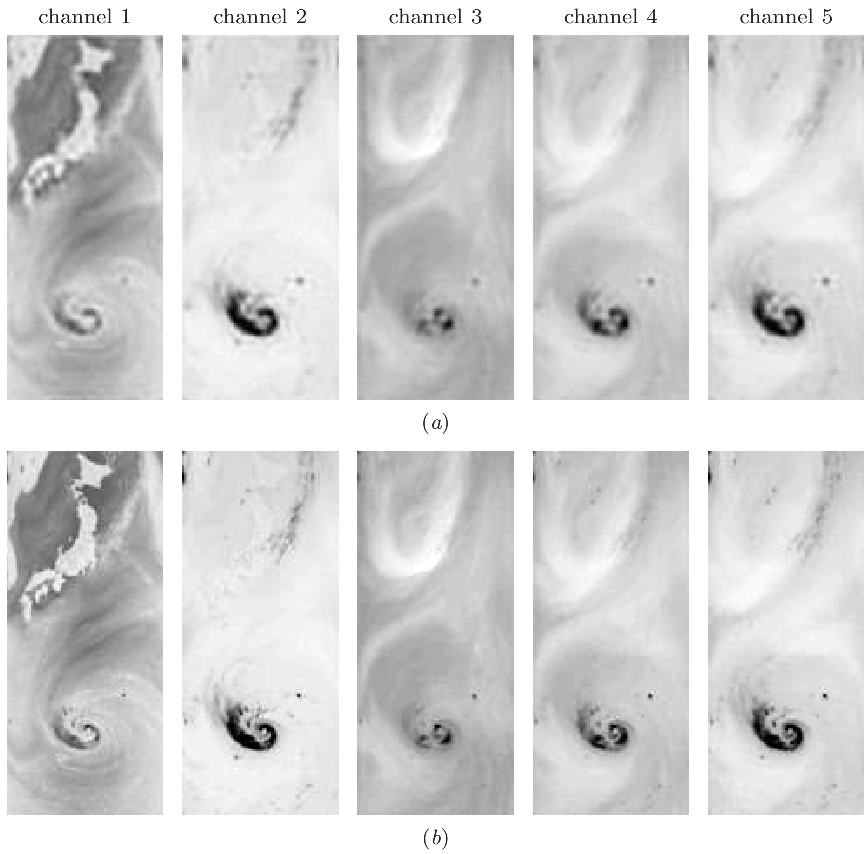

Figure 12. Multispectral reconstruction of channels capturing tropical cyclone Talim. (a) Original microwave channels from Figure 9(c) are convolved with GeoSTAR kernel from Figure 3. (b) Reconstructed images.

Here, the weighting constants ω_k are calculated using the total variation (TV) averaging (Marquina and Osher 2008; Jung, Marquina, and Vese 2009, 2013). Minimization problem (11) can be re-written as

$$\min_{\boldsymbol{u}} \quad ||\boldsymbol{u}||_{\mathrm{MTV}} + \frac{\mu}{2}||K * \boldsymbol{u} - \bar{\boldsymbol{f}}||_2^2, \tag{12}$$

where $\bar{\boldsymbol{f}} = \sum_k \omega_k \boldsymbol{f}_k$ is the weighted TV mean of the observations $\boldsymbol{f}_k$. Fast multispectral Split Bregman deconvolution, described in the previous section, is applied to (12).

Figure 13 displays a conceptual diagram and Figure 14 shows the multiframe super-resolution results. As displayed in Figure 13, a physical scene is consecutively blurred with a noisy GeoSTAR PSF corrupted with 10% visibility error to produce a multiframe image sequence. The average signal-to-noise ratio of an image in the corrupted sequence is 35.48, and the average RMS error is 16.98. Super-resolution reconstruction results are shown in Figure 14 for cases when 1, 2, 3, 5, 10, and 20 frames are used. Table 3 shows RMS errors and signal-to-noise ratios of the reconstructed images. As expected, the quality of the reconstruction increases with the number of images in a sequence.

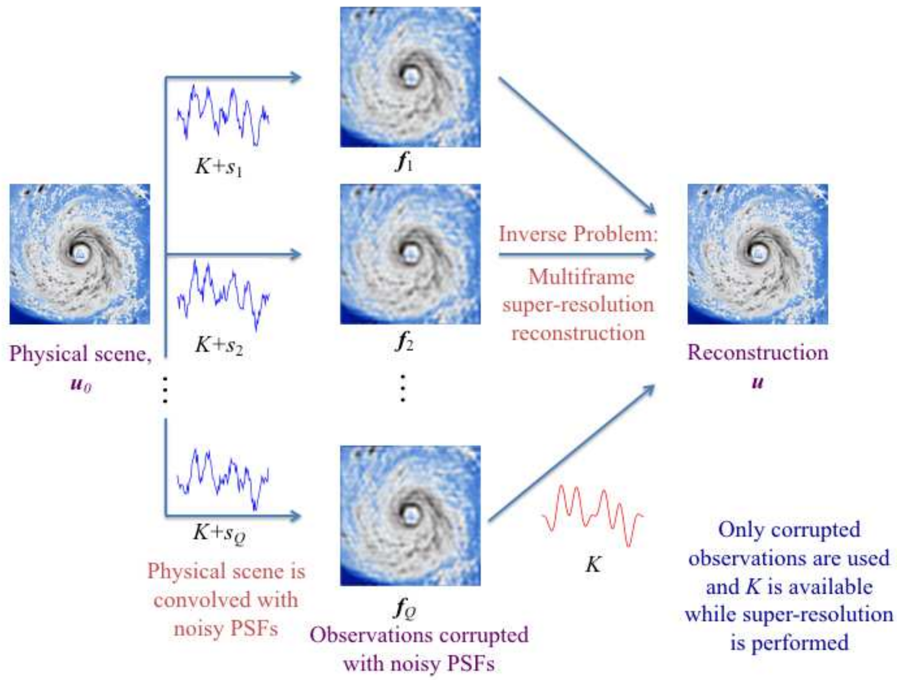

Figure 13. Conceptual diagram of multiframe super-resolution process. A depiction of a physical scene, when captured, is convolved by the PSF K, degraded by a different noise function s_k, to arrive at the observation f_k. The super-resolution algorithm reconstructs image u from multiple observations.

Table 3. Root mean square errors and signal-to-noise ratios in six-channel reconstructed images after multispectral multiframe reconstruction was performed. Results are shown in Figure 14. For initial frames, RMS errors are 16.98, and SNR values are 35.48, on average.

Number of frames	RMSE	SNR
1	17.80	35.07
2	12.85	37.90
3	11.29	39.02
5	10.11	39.98
10	8.93	41.06
20	8.41	41.58

5. Conclusion and Future Work

We developed efficient multispectral deconvolution methodology and applied these techniques to reduce image blurring and distortion inherent in an aperture synthesis system. Unlike the conventional linear apodization approach, our process reduces not only the ringing within the image, but also significantly reduces the errors in the overall image.

There are several paths for future research. The most obvious one is to account for physical deformation in consecutive frames while the scene is being captured. Ongoing and future work will also involve a study of performing simultaneous upsampling and deconvolution on real data. Finally, we plan to combine multiframe, multispectral, and simultaneous upsampling and deconvolution into a single computational framework.

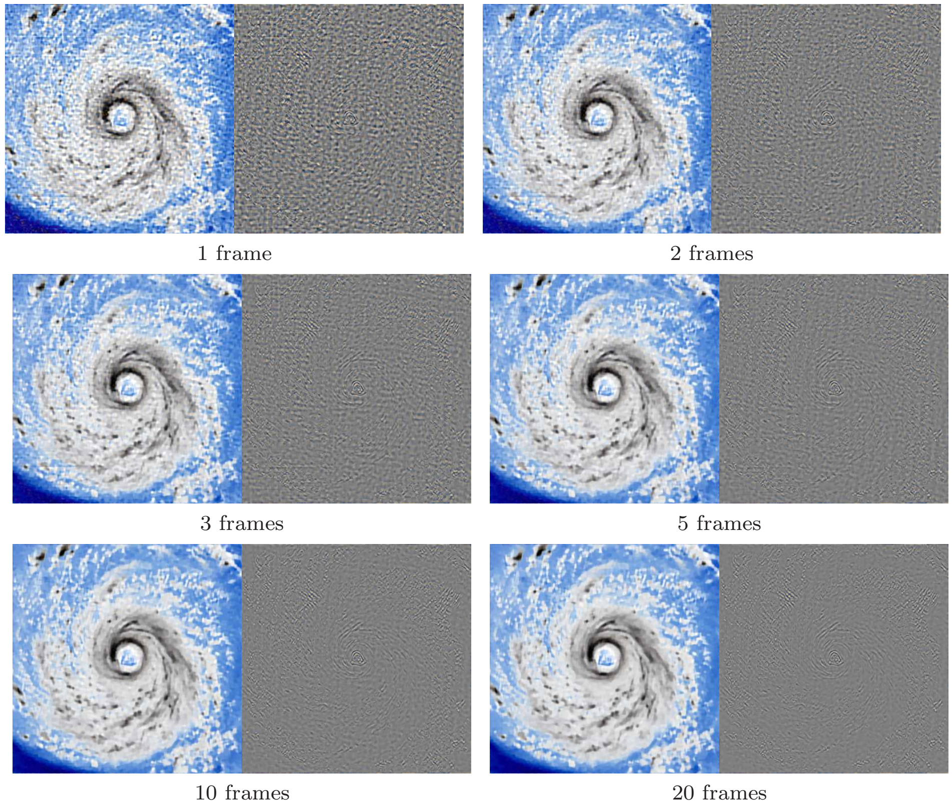

Figure 14. Mulstispectral multiframe super-resolution results. Clean 6-channel image of Figure 2 is consecutively blurred with noisy PSF (see Figure 13) to produce an image sequence. Super-resolution reconstruction results along with corresponding errors are shown for cases when 1, 2, 3, 5, 10, and 20 frames are used. SNR and RMSE values for reconstructed images are listed in Table 3.

5.1. *Funding*

The research was carried out at the Jet Propulsion Laboratory, California Institute of Technology, under a contract with the National Aeronautics and Space Administration. IY also acknowledges support from the National Science Foundation Grant DMS 1217239.

References

Buades, A., B. Coll, and J. M. Morel. 2005. “A Review of Image Denoising Algorithms, with a New One.” *SIAM J. Multi. Model. & Simul.* 4 (2): 490–530.

Donoho, David L., and Iain M. Johnstone. 1995. “Adapting to unknown smoothness via wavelet shrinkage.” *Journal of The American Statistical Association* 90 (432): 1200–1224.

Gabay, D., and B. Mercier. 1976. “A dual algorithm for the solution of nonlinear variational problems via finite element approximations.” *Computers and Mathematics with Applications* 2: 17–40.

Gilboa, G., and S. Osher. 2007. “Nonlocal Linear Image Regularization and Supervised Segmentation.” *SIAM J. Multi. Model. & Simul.* 6 (2): 595–630.

Gilboa, G., and S. Osher. 2008. “Nonlocal Operators with Applications to Image Processing.” *SIAM J. Multi. Model. & Simul.* 7 (3): 1005–1028.

Glowinski, R., J. L. Lions, and R. Tremolieres. 1981. *Numerical Analysis of Variational Inequalities*. Amsterdam, New York, Oxford: North-Holland.

Glowinski, R., and A. Marrocco. 1975. "Sur l'approximation, par elements finis d'ordre un, et la resolution, par, penalisation-dualité, d'une classe de problems de Dirichlet non lineares." *Revue Française d'Automatique, Informatique, et Recherche Opérationelle* 9: 41–76.

Goldstein, T., and S. Osher. 2009. "The Split Bregman Method for L1-Regularized Problems." *SIAM Journal on Imaging Sciences* 2 (2): 323–343.

Guo, Weihong, and Wotao Yin. 2012. "Edge Guided Reconstruction for Compressive Imaging." *SIAM Journal on Imaging Sciences* 5 (3): 809–834.

Jung, Miyoun, Xavier Bresson, Tony F. Chan, and Luminita A. Vese. 2009. "Color Image Restoration Using Nonlocal Mumford-Shah Regularizers." *Lecture Notes in Computer Science* 5681: 373–387.

Jung, Miyoun, Xavier Bresson, Tony F Chan, and Luminita A Vese. 2011. "Nonlocal Mumford-Shah regularizers for color image restoration." *IEEE Transactions on Image Processing* 20 (6): 1583–1598.

Jung, M., A. Marquina, and L. Vese. 2009. "Multiframe image restoration in the presence of noisy blur kernel." *IEEE International Conference on Image Processing* 1529–1532.

Jung, Miyoun, Antonio Marquina, and Luminita A. Vese. 2013. "Variational Multiframe Restoration of Images Degraded by Noisy (Stochastic) Blur Kernels." *J. Comput. Appl. Math.* 240: 123–134.

Kindermann, S., S. Osher, and P. Jones. 2005. "Deblurring and Denoising of Images by Nonlocal Functionals." *SIAM J. Multi. Model. & Simul.* 4 (4): 1091–1115.

Lou, Yifei, Xiaoqun Zhang, Stanley Osher, and Andrea L. Bertozzi. 2010. "Image Recovery via Nonlocal Operators." *J. Sci. Comput.* 42 (2): 185–197.

Marquina, A., and S. Osher. 2008. "Image Super-Resolution by TV-Regularization and Bregman Iteration." *J. Sci. Comput.* 37: 367–382.

Michalakes, J., J. Dudhia, D. Gill, J. Klemp, and W. Skamarock. 1998. *Design of a next-generation regional weather research and forecast model: Towards Teracomputing*. River Edge, New Jersey: World Scientific.

Mumford, David, and Jayant Shah. 1989. "Optimal Approximations by Piecewise Smooth Functions and Associated Variational Problems." *Communications on Pure and Applied Mathematics* 42: 577–685.

Osher, S., M. Burger, D. Goldfarb, J. Xu, and W. Yin. 2005. "An Iterative Regularization Method for Total Variation-Based Image Restoration." *Multiscale Modeling & Simulation* 4 (2): 460–489.

Peyré, Gabriel. 2008. "Image Processing with Nonlocal Spectral Bases." *Multiscale Modeling & Simulation* 7 (2): 703–730.

Rudin, L., S. Osher, and E. Fatemi. 1992. "Nonlinear Total Variation Based Noise Removal Algorithms." *Physica D* 60: 259–268.

Szlam, Arthur D., Mauro Maggioni, and Ronald R. Coifman. 2008. "Regularization on Graphs with Function-adapted Diffusion Processes." *Journal of Machine Learning Research* 9: 1711–1739.

Tanner, A.B., and C.T. Swift. 1993. "Calibration of a synthetic aperture radiometer." *IEEE Transactions on Geoscience and Remote Sensing* 31 (1): 257–267.

Tanner, A.B., W.J. Wilson, B.H. Lambrigsten, S.J. Dinardo, S.T. Brown, P.P. Kangaslahti, T.C. Gaier, et al. 2007. "Initial Results of the Geostationary Synthetic Thinned Array Radiometer (GeoSTAR) Demonstrator Instrument." *IEEE Transactions on Geoscience and Remote Sensing* 45 (7): 1947–1957.

Wang, Y., J. Yang, W. Yin, and Y. Zhang. 2008. "A new alternating minimization algorithm for total variation image reconstruction." *SIAM Journal on Imaging Sciences* 1 (3): 248–272.

Wang, Yilun, Wotao Yin, and Yin Zhang. 2007. "A Fast Algorithm for Image Deblurring with Total Variation Regularization." *CAAM Technical Report* TR07-10.

Yang, J., W. Yin, Y. Zhang, and Y. Wang. 2009. "A Fast Algorithm for Edge-Preserving Variational Multichannel Image Restoration." *SIAM Journal on Imaging Sciences* 2 (2): 569–592.

Yang, J., Y. Zhang, and W. Yin. 2009. "An Efficient TVL1 Algorithm for Deblurring

Multichannel Images Corrupted by Impulsive Noise." *SIAM J. Sci. Comput.* 31 (4): 2842–2865.

Yang, Junfeng, Yin Zhang, and Wotao Yin. 2010. "A Fast Alternating Direction Method for TVL1-L2 Signal Reconstruction From Partial Fourier Data." *Selected Topics in Signal Processing, IEEE Journal of* 4 (2): 288–297.

Yanovsky, Igor, Bjorn Lambrigtsen, Alan Tanner, and Luminita Vese. 2015. "Efficient Deconvolution and Super-Resolution Methods in Microwave Imagery." *IEEE Journal of Selected Topics in Applied Earth Observations and Remote Sensing* 8 (9): 4273–4283.

Yin, W., S. Osher, D. Goldfarb, and J. Darbon. 2008. "Bregman Iterative Algorithms for L1-Minimization with Applications to Compressed Sensing." *SIAM Journal on Imaging Sciences* 1 (1): 143–168.